Intersubband electron-electron scattering in asymmetric quantum wells designed for far-infrared emission

P. Kinsler,* P. Harrison, and R. W. Kelsall
Institute of Microwaves and Photonics, School of Electronic and Electrical Engineering, University of Leeds, LS2 9JT, United Kingdom
(Received 17 March 1998)

Population inversion in inter-subband emitters and lasers depends critically on the lifetimes of the nonradiative inter-subband transitions. We find that the often neglected Auger-type processes and Pauli exclusion effects can dominate the electron-electron scattering contributions to the total scattering rate. Electron exchange is also considered. In a range of three-level asymmetric quantum-well structures designed to produce terahertz radiation, we estimate the potential for laser operation for a range of electron densities and temperatures using the population ratio τ_{32}/τ_{21}. We find that predicted population ratios have a strong dependence on the electron-electron scattering rates, and that Auger processes and Pauli exclusion are of particular importance. In addition, the temperature dependence of the population ratio is significantly altered by the inclusion of electron-electron scattering processes. Our results indicate that the interplay of electron-phonon and electron-electron scattering rates suggest optimum operating temperatures for different emitter frequencies. [S0163-1829(98)03032-X]

I. INTRODUCTION

Recently there has been much progress in the development of midinfrared quantum cascade lasers, including increased output power and higher operating temperatures.[1] There are many applications that could benefit from extending the frequency range into the far infrared or terahertz range (300–300 μm, 1–10 THz). Example applications are those that make use of the smaller antenna sizes and greater bandwidths, such as mobile telephones, wireless computer networks and high resolution radar.[2]

When designing a far infrared intersubband laser using GaAs technology, the required emission frequency (which is determined by the subband spacing) is smaller than the LO phonon energy of 36 meV (8.7 THz, 34 μm). This seems initially to be a great advantage, as LO emission should therefore be suppressed relative to the desired radiative emission. However, increasing temperature broadens the energy distribution of the subband populations, resulting in only partial suppression, since LO phonon emission from the more energetic electrons is allowed.[3,4] Electron-electron scattering is also enhanced by the smaller subband separation, an effect that is often ignored when considering these devices.

In this paper we study the effects of electron-electron scattering[5,6] in optically pumped intersubband terahertz emitters at the likely operating electron densities of 100×10^{10} cm^{-2}. Lower densities are less practical as they make it more difficult to pump sufficient population into the upper laser levels and obtain enough gain. The prototype terahertz emitter devices we use are based on the asymmetric quantum-well structures first suggested by Berger,[7] and developed further by Harrison and Kelsall.[4] The theoretical part of our electron-electron scattering calculations in Sec. II include determining the final momentum states of the electrons, which allows us to include the effects of Pauli exclusion and electron exchange.[8,9] In Sec. III this theory is used to investigate the practical effects of the important Auger-type intersubband processes, which are forbidden by selection rules in symmetric wells. This section also includes a study of Pauli exclusion due to subband filling in the set of prototype terahertz devices. In Sec. IV we analyze in detail the performance of the prototype devices for a range of subband spacings, electron densities, and temperatures. The results show that, in contrast to previous calculations, which considered only electron-phonon scattering, inversion is reduced by increasing the electron density. Also we see an optimum choice of operating temperature for any given emitter frequency (subband spacing).

II. THEORY

The quantum-well structures considered in this paper were designed for optically excited intersubband terahertz emission. Intersubband optical pumping has recently been demonstrated by Julien and co-workers.[10,11] For commercial applications optical pumping is less convenient than electrical injection, but compared to quantum cascade lasers it allows great simplifications in device design and fabrication. We use the set of three level prototype devices from Harrison and Kelsall[4] (see Table I and Fig. 1). An asymmetric potential is required to break the even parity of the $|1\rangle$ and $|3\rangle$ subband wave functions, and hence permit the $|1\rangle \rightarrow |3\rangle$ optical pump transition. These structures consist of a 65-Å GaAs deep well layer with an adjacent $Ga_{1-x}Al_xAs$ step ($x \in [0.12,0.18]$), between thick $Ga_{0.76}Al_{0.24}As$ barriers. Optical pumping with a 10.6-μm CO_2 laser is used as the means used to excite electrons from the lowest energy subband $|1\rangle$ to the highest subband $|3\rangle$; the aim is to create a population inversion between the third $|3\rangle$ and the second subband $|2\rangle$. The separation of the third and second subbands is tuned for terahertz emission.

The energy levels and wave functions of the quantum wells were obtained by numerical solution of the effective

TABLE I. Structural parameters of the three-level asymmetric quantum well with a terahertz intersubband separation (E_3-E_2).

Step x_b (%)	Step width b (Å)	E_3-E_1 (meV)	E_3-E_2 (meV)	E_3-E_2 (THz)	τ_{32}^{rad} (μs)
10	101	116.988	49.851	12.1	0.18
11	105	117.321	45.708	11.1	0.21
12	111	117.117	41.119	9.9	0.23
13	118	117.154	36.504	8.8	0.27
14	127	117.179	31.750	7.7	0.32
15	140	116.899	26.695	6.5	0.39
16	157	116.902	21.684	5.2	0.49
17	182	116.992	16.612	4.0	0.66
18	224	117.143	11.454	2.8	0.99

mass Schrödinger equation.[12] The population distributions of electrons and phonons were described by Fermi-Dirac and Bose-Einstein distributions respectively, and it was assumed that both electron and phonon temperatures for any electron subband or phonon type were the same as the lattice temperature. For computational reasons the distributions were truncated at either $23k_BT$ above the largest subband energy in a given calculation, or at the top of the well. Electrons with total energy greater than the barriers were assumed to escape immediately and play no further part in scattering events. As each subband has its own electron density, it also has its own corresponding Fermi level.

The numerical wave functions were then used to calculate electron-phonon scattering rates using Fermi's ''golden rule.''[13] The electron-phonon scattering rates included the polar LO phonon and acoustic (deformation potential) modes. A range of temperatures from 2 to 300 K was considered, so we do not use the usual high-temperature (equipartition) or low-temperature (zero point) approximations.[14] A constant LO phonon energy was used, and the computing time for the acoustic phonon scattering calculations was reduced by assuming a fixed phonon energy of 2 meV. Bulk-like phonon modes were assumed for both acoustic and LO phonon scattering. Since the main purpose of this paper is to study electron-electron scattering, a detailed description of confined phonon modes[15,16] is deferred to subsequent work.

Electron-electron scattering events are denoted using the indices $ijfg$, where i and j are the subbands of the initial electron states with in-plane momenta $k_i=|\mathbf{k_i}|$ and $k_j=|\mathbf{k_j}|$. The angle between $\mathbf{k_i}$ and $\mathbf{k_j}$ is denoted α (see Fig. 2). Similarly, f and g are the subbands of the final electron states, with in-plane momenta $\mathbf{k_f}$ and $\mathbf{k_g}$.

In S.I. units, the electron-electron scattering rate ignoring spin can be written as[5,6]

$$
\begin{aligned}
&W_{ijfg}(k_i,\sigma)\\
&\quad=\frac{e^4}{\hbar(4\pi\epsilon_r\epsilon_0)^2}\int dk_j\int d\alpha\int d^2k_f\\
&\qquad\times\int d^2k_g\left[\frac{|A_{ijfg}(q_\perp)|^2}{q_\perp^2\epsilon_{sc}^2(q_\perp^2)}f_j(k_j)[1-f_f(\mathbf{k_f})]\right.\\
&\qquad\times[1-f_g(\mathbf{k_g})]\delta[E_f(\mathbf{k_f})+E_g(\mathbf{k_g})-E_i(\mathbf{k_i})-E_j(\mathbf{k_j})]\\
&\qquad\left.\times\delta(\mathbf{k_f}+\mathbf{k_g}-\mathbf{k_i}-\mathbf{k_j})\right],
\end{aligned}
\tag{2.1}
$$

where ϵ_{sc} is the temperature-dependent dielectric function, which is calculated by assuming static single subband screening of the electron-electron interaction within the random phase approximation (RPA).[17,18] More sophisticated dynamic screening calculations can be done (see, e.g., Ref. 19), but the need to obtain a self-consistent solution means that the computer time required was impractically long for use in our calculations. The electron distribution functions are denoted by f_κ, where κ is one of $\{i,j,f,g\}$, and are taken to be Fermi-Dirac distributions that depend on the subband Fermi

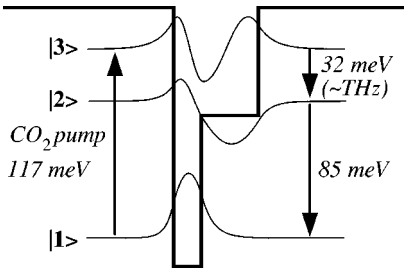

FIG. 1. Diagram of the energy levels and wave functions of a three-level asymmetric quantum well. The energy spacing E_3-E_1 between subband $|3\rangle$ and subband $|1\rangle$ is tuned for CO_2 pumping, and terahertz emission is sought from the $|3\rangle$ to $|2\rangle$ transition (7.7 THz in this example).

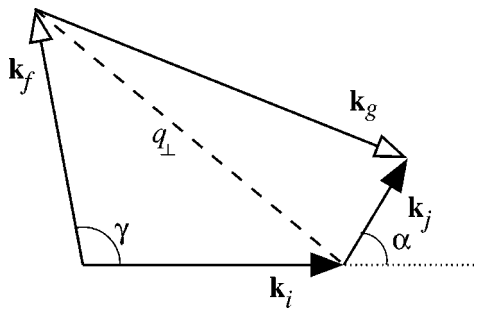

FIG. 2. Diagram of the initial and final electron momenta, showing the angles used in the calculations. $\mathbf{k_i}$ and $\mathbf{k_j}$ (with the filled arrowheads) are the momenta of the electrons before scattering, and $\mathbf{k_f}$ and $\mathbf{k_g}$ (open arrowheads) are the momenta of the electrons afterwards.

energies $E_{F\kappa}$, which in turn depend on the subband carrier densities n_κ. The $A_{ijfg}(q_\perp)$ are the form factors given by the overlap of the wave functions from the initial and final states.[5,6]

Smet, Fonstad, and Hu[6] evaluated the electron-electron scattering rate by defining an angle θ that parametrizes the momentum variable $q_\perp$. The Pauli exclusion factors $[1-f_f(k_f)][1-f_g(k_g)]$ were neglected to obtain a scattering rate, which is a good approximation when electron densities in the final states are low. However, at higher densities the effects of $f_f(\mathbf{k_f})$ and $f_g(\mathbf{k_g})$ may be significant and should be included. To investigate Pauli exclusion effects we solve for the momentum and energy conservation rules for the electron-electron scattering events

$$\mathbf{k_i}+\mathbf{k_j}=\mathbf{k_f}+\mathbf{k_g}, \tag{2.2}$$

$$E_i+\frac{\hbar^2\mathbf{k_i}\cdot\mathbf{k_i}}{2m^*}+E_j+\frac{\hbar^2\mathbf{k_j}\cdot\mathbf{k_j}}{2m^*}=E_f+\frac{\hbar^2\mathbf{k_f}\cdot\mathbf{k_f}}{2m^*}+E_g+\frac{\hbar^2\mathbf{k_g}\cdot\mathbf{k_g}}{2m^*}. \tag{2.3}$$

We eliminate $\mathbf{k_g}$ using momentum conservation [Eq. (2.2) inserted into Eq. (2.3)], and solve the resulting quadratic in $|\mathbf{k_f}|$ to get

$$\begin{aligned}|\mathbf{k_f}|=&[|\mathbf{k_i}|\cos(\gamma)+|\mathbf{k_j}|\cos(\alpha-\gamma)]\\&\pm\{[|\mathbf{k_i}|\cos(\gamma)+|\mathbf{k_j}|\cos(\alpha-\gamma)]^2\\&-4|\mathbf{k_i}||\mathbf{k_j}|\cos(\alpha)+\Delta^2\}^{1/2},\end{aligned} \tag{2.4}$$

where γ is the angle between $\mathbf{k_i}$ and $\mathbf{k_f}$ and $\Delta^2=(4m^*/\hbar^2)(E_i+E_j-E_f-E_g)$. The relationship between these vectors is shown on Fig. 2. Since we now know $\mathbf{k_f}$ (from $|\mathbf{k_f}|$ and γ), we can find the corresponding $\mathbf{k_g}$ from the vector diagram, which gives

$$\begin{aligned}|\mathbf{k_g}|=&\{[|\mathbf{k_i}|+|\mathbf{k_j}|\cos(\alpha)-|\mathbf{k_f}|\cos(\gamma)]^2\\&+[|\mathbf{k_j}|\sin(\alpha)-|\mathbf{k_f}|\sin(\gamma)]^2\}^{1/2}.\end{aligned} \tag{2.5}$$

The momentum variable $q_\perp$ can be found using the cosine rule, and is

$$q_\perp^2=\mathbf{k_i}\cdot\mathbf{k_i}+\mathbf{k_f}\cdot\mathbf{k_f}-2|\mathbf{k_i}||\mathbf{k_f}|\cos(\gamma). \tag{2.6}$$

Using these the scattering rate becomes

$$\begin{aligned}W_{ijfg}(k_i,\sigma)=&\frac{e^4}{\hbar(4\pi\epsilon_r\epsilon_0)^2}\int dk_j\int d\alpha\int dC(\gamma)\\&\times\left[\frac{|A_{ijfg}(q_\perp)|^2}{q_\perp^2\epsilon_{sc}^2(q_\perp^2)}f_j(k_j)[1-f_f(\mathbf{k_f})]\right.\\&\left.\times[1-f_g(\mathbf{k_g})]\right],\end{aligned} \tag{2.7}$$

where $C(\gamma)$ is the contour formed from the allowed final states (see Fig. 3) as parametrized by the angle γ. These allowed final states are those that satisfy only the energy and momentum conservation conditions. Note that the angle θ seems to be a better way to parametrize C—an integral advancing equal angular steps in θ covers C evenly because the origin of θ is at its center. However, the analytic expressions required to work out k_g from θ are more complicated.

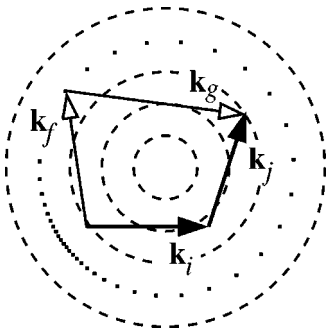

FIG. 3. Allowed final-state contours for a range of intersubband energies $\Delta^2=(4m^*/\hbar^2)(E_i+E_j-E_f-E_g)$, as indicated by the dashed lines. Larger values of Δ^2 correspond to the bigger circles. The allowed final states are traced out as the vertex of the $\mathbf{k_f}$, $\mathbf{k_g}$ arrows (open arrowheads) moves around the circular contour. The dotted curve indicates how equal steps in the angle γ between $\mathbf{k_i}$ and $\mathbf{k_f}$ (filled arrowheads) trace out the contour of allowed final states.

When including electron spin, the exchange effect must also be considered. This is relevant to collisions of electron pairs of the same spin, when an interference occurs between the two indistinguishable scattering events that involve same-spin electrons. If we assume identical distributions and equal densities for both spin-up and spin-down electrons, the following replacement in Eq. (2.7) should be made:[8,9]

$$\begin{aligned}\frac{|A_{ijfg}(q_\perp)|^2}{q_\perp^2\epsilon_{sc}^2(q_\perp^2)}\rightarrow\frac{1}{2}\left[\frac{|A_{ijfg}(q_\perp)|^2}{q_\perp^2\epsilon_{sc}^2(q_\perp^2)}+\frac{|A_{ijgf}(q_\perp')|^2}{q_\perp'^2\epsilon_{sc}^2(q_\perp'^2)}\right.\\\left.-\frac{A_{ijfg}(q_\perp)A_{ijgf}^*(q_\perp')}{q_\perp q_\perp'\epsilon_{sc}(q_\perp^2)\epsilon_{sc}(q_\perp'^2)}\right],\end{aligned} \tag{2.8}$$

where $\mathbf{k_f}'=\mathbf{k_g}$ and $\mathbf{k_g}'=\mathbf{k_f}$ so that

$$q_\perp'^2=\mathbf{k_j}\cdot\mathbf{k_j}+\mathbf{k_f}\cdot\mathbf{k_f}-2|\mathbf{k_j}||\mathbf{k_f}|\cos(\alpha-\gamma). \tag{2.9}$$

The Fermi factors in the scattering rate [Eq. (2.1)] are unaffected, since the product $[1-f_f(\mathbf{k_f})][1-f_g(\mathbf{k_g})]$ is unaltered under exchange.

III. ELECTRON-ELECTRON SCATTERING RATES

In this section we summarize the various types of electron-electron scattering processes, and their significance in terms of quantum-well structures. Broadly speaking, there are two types of scattering—''symmetrical'' and ''Auger'' processes. In symmetrical structures, the allowed scattering events are these ''symmetrical'' processes, in which both electrons change up or down by one subband [see Fig. 4(a)]. The other type (Auger), where again two electrons scatter but only one changes up or down by a single subband, is forbidden by selection rules. The selection rules are conditions on the allowed transitions that derive from the even or odd parity of the initial- and final-state electron wave functions, as well as the parity of the interaction between them. However, asymmetric structures do not have electron wave functions with a well-defined parity, so these selection rules are broken

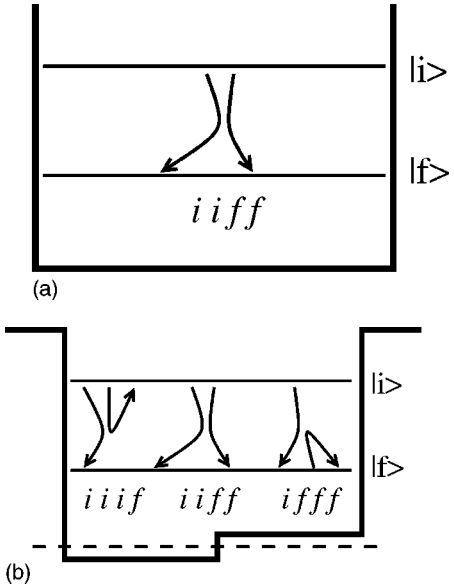

FIG. 4. Schematic diagrams showing the allowed intersubband electron-electron scattering processes for (a) symmetric and (b) asymmetric quantum wells. The *iiif* and *ifff* processes are Auger processes that transfer one electron between subbands.

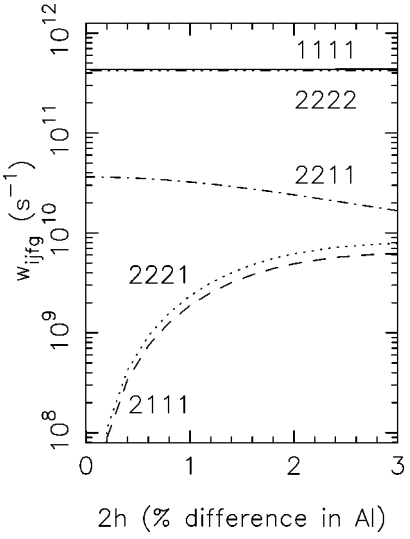

FIG. 5. The effect of asymmetry on electron-electron scattering rates for a quantum well with $n_1=n_2=10^{10}$ cm^{-2} at $T=2$ K. The well has $Ga_{0.72}Al_{0.28}As$ barriers and two side-by-side well layers of $Ga_{0.92\pm h}Al_{0.08\mp h}As$, both 100 Å thick.

and Auger processes can contribute to scattering. For example, in a symmetric well, transfer of population between the second $|2\rangle$ and first $|1\rangle$ subband occurs only by the 2211 process, as the 2111 and 2221 are forbidden. However, in an asymmetric well [Fig. 4(b)], in addition to the 2211 process, which transfers *two* electrons, the 2111 and 2221 processes are also active and transfer an additional one electron each. When working out total population transfer rates between subbands, all three scattering processes and the number of electrons each transfers needs to be taken into account. Note that the Auger processes also include scattering events between electrons in different subbands, e.g., 3121.

The symmetrical processes (e.g., 2211) were described by Smet, Fonstad, and Hu[6] in the low electron density limit where the Pauli exclusion is negligible. We also calculated these rates in an infinite square well whose other parameters were similar to those of a GaAs quantum well—Fig. 4(a) shows a system similar to that used for the results, where the allowed 2211 scattering process between the two lowest subbands is indicated schematically (as *iiff*). Briefly, our allowed 2211 rate calculations also showed the expected decrease in scattering rates with intersubband separation (e.g., as in Ref. 6).

We have also compared calculations of electron-electron scattering rates with and without the exchange terms described in the previous section. In all the cases relevant to the results presented here, the differences were negligible—in contrast to Ref. 8. Consequently we do not show explicit comparisons between the with-exchange and without-exchange cases. However, at the typical operating electron densities of about 100×10^{10} cm^{-2}, Auger processes are always significant, as is Pauli exclusion.

A. Auger intersubband scattering processes

In asymmetric quantum wells, the Auger processes such as 2111 and 2221 can and do contribute to population transfer between subbands. In fact, in our prototype terahertz designs the 2111 scattering rate dominates over the similar 2221 and 2211 rates. Further, there are processes such as 3121 that can contribute significantly despite the large E_3-E_1 subband separation.

To show the effect of asymmetry in a simpler system similar to that of the prototype terahertz devices considered in this paper, consider a set of stepped quantum wells, with half the well deeper, and half shallower than a fixed average value. We increase the asymmetry by increasing the disparity in the aluminum concentration. Figure 4(b) shows schematically a system similar to that used for these results, with the allowed electron-electron scattering processes indicated [here $i=2$(or 3), and $f=1$(or 2)]. The significance of the Auger rates as the asymmetry increases [up to a 3% change ($2h=0.03$) in aluminum concentration] is clearly seen in Fig. 5. Clearly, even if we designed a prototype with a small asymmetry, the Auger rates would still be comparable to the symmetric rates. The intrasubband 1111 and 2222 rates remain unaffected by the asymmetry, but the 2211 rate decreases slowly as the wave-function overlap changes. In contrast, the Auger rates 2221 and 2111 are initially zero, but increase rapidly with asymmetry to within a factor of two of the 2211 rate. There is no significant change in the subband energies for the range of step heights considered here, hence the changes in the scattering rates are due only to changes in the wave functions.

These Auger processes also have a significant effect in the prototype terahertz devices as well. In Fig. 6, all the $|3\rangle\rightarrow|2\rangle$ and $|2\rangle\rightarrow|1\rangle$ intersubband rates are shown for $\Sigma_i n_i=100\times10^{10}$ cm^{-2}. For the $|3\rangle\rightarrow|2\rangle$ rates, the 3121 process clearly dominates. Similarly, for the $|2\rangle\rightarrow|1\rangle$ rates, the 2111 rate is two orders of magnitude greater than the 2211, and so is by far the most significant contributor to electron-electron depopulation of the lower emitter subband over the entire range of structures. The results for higher temperatures are similar and so are not included here. These 3121 and 2111 Auger processes are still significant even at much lower total

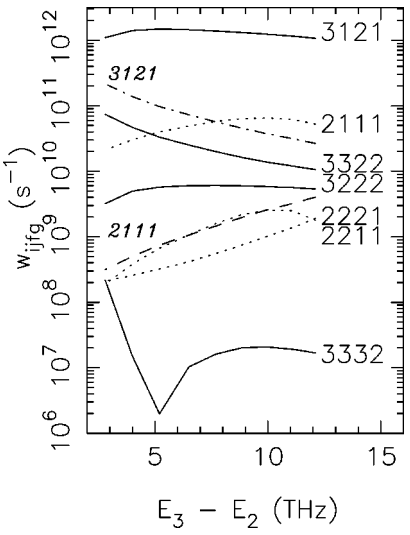

FIG. 6. A comparison of the electron-electron scattering rates, including the Auger rates, of the quantum well structures in Table I. Solid lines are for the $|3\rangle \rightarrow |2\rangle$ processes, dotted lines are for $|2\rangle \rightarrow |1\rangle$. These are at 2 K, with $n_1+n_2+n_3=100\times10^{10}$ cm^{-2} and $n_2=n_3=10^{10}$ cm^{-2}. Also shown are the 3121 (dash-dotted) and 2111 (dashed) rates for $n_1=n_2=n_3=10^{10}$ cm^{-2}.

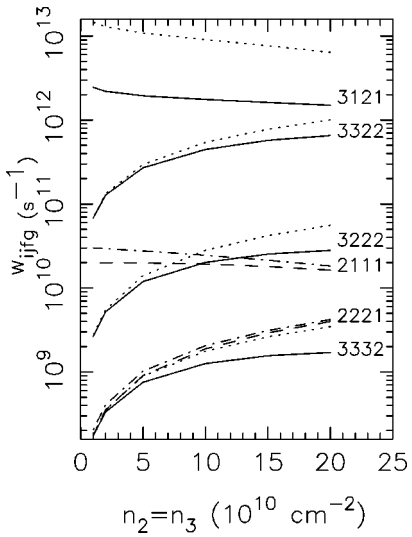

FIG. 7. Intersubband electron-electron scattering rates, comparing the exact rates (solid lines and dashed lines) with those from calculations ignoring the Pauli exclusion effect (dotted and dash-dotted lines). This is for the three-level prototype structure with a 2.8-THz emission energy, $\Sigma n_i=100\times10^{10}$ cm^{-2}, $n_2=n_3$, and $T=77$ K.

electron densities ($\Sigma n_i=3\times10^{10}$ cm^{-2}), as indicated by the dashed and dot-dashed curves in Fig. 6.

B. Pauli exclusion effect

In the low carrier density limit we can justifiably ignore any Pauli exclusion effects. However, a practical laser device will probably need electron densities of around 100×10^{10} cm^{-2} in order to have sufficient gain, and at these high densities Pauli exclusion inhibits scattering into occupied or partially occupied states. This is particularly noticeable for states below the Fermi energy of the final-state subband, where there is a significant probability of occupation. At low temperatures, where the final subband is (almost) completely filled below the Fermi energy, scattering into that lower part of the subband is almost completely suppressed. At higher temperatures the suppression becomes more gradual because the broadened Fermi-Dirac distributions have partially occupied states below the Fermi energy, into which the electrons can scatter.

The Pauli exclusion effect is significant in the asymmetric quantum-well structures used for our prototype terahertz emitters. Intrasubband events affect the form of the electron distribution within each subband, which in turn affects the intersubband rates and is therefore important in device design. Such effects lie beyond the scope of this work but could be accounted for by using a Monte Carlo simulation. Calculations also demonstrate that Pauli exclusion can reduce the intrasubband scattering rates by up to 40% for the higher subbands. For the lowest subband, the actual 1111 rate for $n_1\sim100\times10^{10}$ cm^{-2} is more than one order of magnitude slower than what would be calculated without allowing for the Pauli exclusion effect.

Figure 7 shows the effects of Pauli exclusion for the intersubband $|2\rangle \rightarrow |1\rangle$ and $|3\rangle \rightarrow |2\rangle$ processes in one of the prototype terahertz devices. The sum of the subband electron densities is again 100×10^{10} cm^{-2}, and the two upper subbands are taken to have the same population, as might be expected in a laser with marginal inversion. The differing trends are due to the redistribution of carriers between the subbands—rates strongly dependent on n_1 decrease as population is shifted into n_2 and n_3, and vice versa. The results for much lower densities (10^{10} cm^{-2}) are not dissimilar, except that the rates are smaller by roughly an order of magnitude, and the effect of Pauli exclusion nearly vanishes.

The asymmetric potential of the quantum well ensures that Auger processes contribute to intersubband population transfer. In this case, the suppression in the 2111 rate caused by Pauli exclusion is about one-third for $n_2=n_3=1$. There are similar reductions in the 3322, 3222, and 3222 scattering rates for large n_3. The most significant reduction is in the important 3121 rate, with the highly populated $|1\rangle$ blocking many scattering events, thus reducing this rate by about an order of magnitude. Clearly, these results show that Pauli exclusion can be a significant effect and cannot be ignored.

IV. POPULATION RATIOS

To examine the potential of the three-level asymmetric quantum well system as a terahertz laser in the light of our new electron-electron scattering calculations, it is necessary to look at the carrier dynamics that govern population inversion. Previous calculations that neglected electron-electron scattering[4] suggested that significant inversion might be easy to achieve in a three subband structure at low temperatures and/or small subband separations. However, the electron-electron scattering is stronger at smaller subband separations, and in particular the 3121 and 2111 Auger scattering processes are very strong for large ground-state populations (e.g., $\sim100\times10^{10}$ cm^{-2}).

The population of the lower laser subband $|2\rangle$ is given by a simple rate equation analysis as

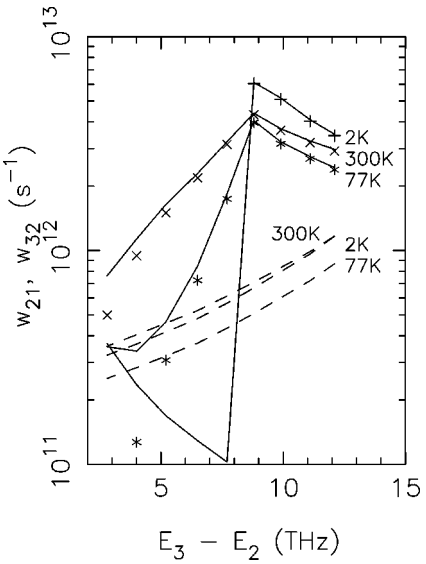

FIG. 8. A comparison of the total electron scattering rates between subbands, for $n_1=n_2=n_3=10^{10}$ cm^{-2}, for 2, 77, and 300 K (as labeled); the symbols indicate the summed rates *excluding* electron-electron scattering for 2 K (+), 77 K (×), and 300 K (∗), respectively. The solid lines show the total rate w_{32} from subband $|3\rangle$ to subband $|2\rangle$. The dashed lines show the total rate w_{21} from subband $|2\rangle$ to subband $|1\rangle$. Below 9 THz (at 2 K) the rates when electron-electron scattering is excluded are lower than the y-axis minimum of 10^{11} s^{-1}.

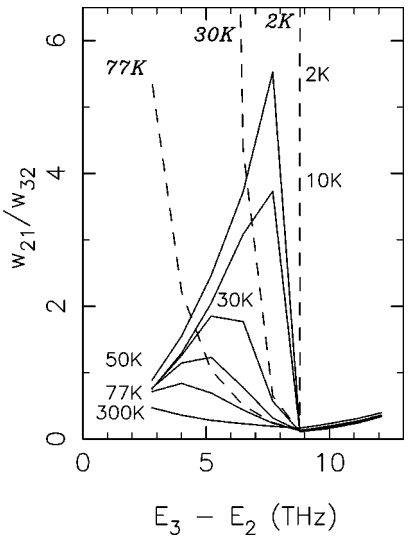

FIG. 9. Predicted population ratios for the range of structures listed in Table I, for $n_i=10^{10}$ cm^{-2}. Results for a range of temperatures are shown by the solid lines. The dashed lines indicate the rates calculated for 2, 30, and 77 K when electron-electron scattering is excluded, clearly showing the importance of including this effect for small subband separations.

$$\frac{dn_2}{dt}=n_3w_{32}-n_2w_{21}, \tag{4.1}$$

where $w_{32}=1/\tau_{32}$ ($w_{21}=1/\tau_{21}$) is the sum of all the radiative, acoustic-phonon, LO-phonon, and electron-electron scattering rates from the third $|3\rangle$ subband to the second $|2\rangle$ subband (or second $|2\rangle$ to first $|1\rangle$). The radiative decay rates are very slow ($\sim 10^6-10^7$ s^{-1}) in comparison to the other rates and can be neglected. At equilibrium there is a steady-state population inversion ($n_3>n_2$) if

$$\frac{1}{\tau_{21}}>\frac{1}{\tau_{32}}. \tag{4.2}$$

The ratio $w_{21}/w_{32}=\tau_{32}/\tau_{21}$ thus gives the ''population ratio'' (n_3/n_2). Note that our scattering rate calculations have assumed equal populations in n_3 and n_2, which is a good starting point as the rates are not too sensitive to the exact electron densities. Only marginal inversions are expected in prototype devices, and so this population ratio can be considered to be a measure of how easy inversion would be to achieve.

Despite the promise of laser operation at useful electron densities suggested by earlier calculations that considered only electron-phonon scattering, we found that the strong 3121 electron-electron scattering process destroys any possibility of attaining $w_{21}/w_{32}>1$, even at low temperatures, for electron densities of $\Sigma n_i=100\times10^{10}$ cm^{-2}. At lower electron densities (10×10^{10} cm^{-2}), we find it is just possible to get $w_{21}/w_{32}>1$ at 2 K, but we have to go down to $\Sigma_i n_i \sim 10^{10}$ cm^{-2} to see the possibility of laser operation for a range of prototypes and temperatures.

Figure 8 shows how the total intersubband scattering rates vary with structure and temperature for $n_i=10^{10}$ cm^{-2}. The graphs both appear qualitatively similar to those including only the phonon scattering.[4] The depopulation rate of the second subband w_{21} is increased by the addition of electron-electron scattering. However, the electron-electron contributions make a significant difference to the $|3\rangle\rightarrow|2\rangle$ rate (w_{32}) for low temperatures and below the LO phonon threshold, as w_{32} now decreases to the electron-electron rate of about 10^{11}–10^{12} s^{-1}—instead of down to the electron–acoustic-phonon rate (at $\sim 10^8-10^9$ s^{-1}).

The effect of these changes in scattering rates is highlighted by Fig. 9. This shows the population ratio w_{21}/w_{32} as a function of the emission energy for the prototype terahertz devices in Table I. The calculations without electron-electron scattering predicted an increase in inversion as E_3-E_2 decreased, with steeper increases for lower temperatures (dashed lines). In comparison, it can be seen that calculations including the electron-electron scattering (solid lines) predict lower population ratios at small E_3-E_2, because of the increased $|3\rangle\rightarrow|2\rangle$ rate.

The inclusion of the 2111 electron-electron scattering process tends to alleviate this reduction in population ratio at large E_3-E_2 separations (above 5 THz), as there the 2111 rate tends to a maximum, while the 3322 rate decreases, especially for lower $\Sigma_i n_i$ (see Fig. 6). This occurs because electron-electron scattering rates are inversely dependent on the subband separation—and the $|3\rangle\rightarrow|2\rangle$ rate decreases with increasing E_3-E_2 while the $|2\rangle\rightarrow|1\rangle$ rate increases with the corresponding decrease in E_2-E_1.

This leaves an interval between this crossover and the LO phonon threshold in the mid to upper-terahertz subband gap where inversion ($w_{21}/w_{32}>1$) will not be suppressed by the addition of electron-electron scattering. However, this is squeezed shut at higher temperatures, as the $|3\rangle\rightarrow|2\rangle$ LO

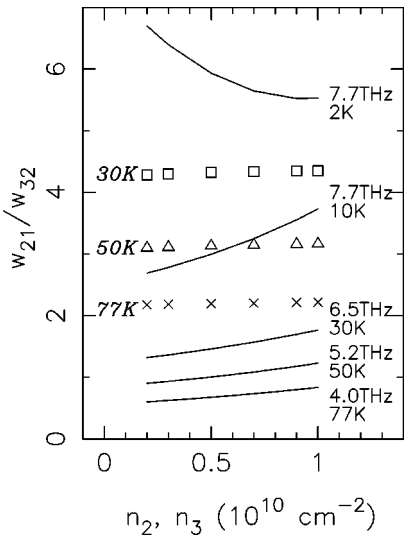

FIG. 10. Predicted population ratios as a function of electron density for the optimum choices of structure and temperature, with $n_i = 10^{10}$ cm^{-2}. The symbols show the results for 30, 50, and 77 K when electron-electron scattering is excluded. The 2- and 10-K results are not shown as they are above the top of the graph.

phonon emission rate starts to increase at subband separations below the LO phonon energy. This can be seen in the w_{32} rate on Fig. 8, as the dip in the 2 K curve between 3 and 8 THz. At 77 K and above the dip has gone, since the temperature-dependent increase in the LO phonon population has increased the LO phonon scattering rates above the $|3\rangle \rightarrow |2\rangle$ electron-electron scattering rate. This in turn directly affects the population ratio.

At 50 K, inversion can still be achieved at emission energies between 4–6 THz, but only to population ratios of a maximum of about 1.2. However, as discussed above, the interval where w_{32} is small gives us the peaks in the population ratios seen on Fig. 9. These peaks indicate that there is an optimum choice of temperature for a given structure, or conversely, an optimum choice of structure for a given temperature.

The effect of Pauli exclusion on these ratios is small. However, for devices operating at higher electron densities (i.e., $>10\times10^{10}$ cm^{-2} the results of Sec. III B show that Pauli exclusion is not insignificant. For $\Sigma n_i = 100\times10^{10}$ cm^{-2} and $n_2 = n_3 = 10^{10}$ cm^{-2} there is a suppression to about two-thirds of the rate without Pauli exclusion (see Fig. 7).

Figure 10 shows how the population ratio depends on the electron distribution between subbands, for the optimum temperature-structure combinations suggested by the peak positions on Fig. 9. In contrast to calculations that neglect electron-electron scattering,[4] the trend is for only slightly changing population ratios as electron density in the upper subbands increases.

Finally, note that all our prototype terahertz devices that can achieve population inversion are unaffected by Restrahl absorption. In both GaAs and AlAs, the Restrahl bands are both very narrow, with the most significant being that at the GaAs TO phonon energy of about 33 meV (or 8 THz). The absorption tails that extend beyond this are very weak, and are negligible even for the prototype operating at 7.7 THz and 2 K.[20]

V. CONCLUSIONS

We have demonstrated the importance not only of including electron-electron scattering in calculations of intersubband transition rates, but also that of considering Auger-type processes and Pauli exclusion effects. These phenomena are particularly significant if the device relies on occurrence of a cutoff in the LO-phonon scattering rates for subband gaps less than the LO-phonon energy.

Auger processes were vital in understanding the electron-electron scattering rates. Most dramatically, the 3121 scattering rate dominated the electron-electron contribution to the total rate w_{32} between subbands $|3\rangle$ and $|2\rangle$. At the electron densities we would hope to use in a practical device, this process extinguished any possibility of achieving inversion, even at low temperatures. Only at reduced densities was a population ratio greater than one attainable. This means that these three subband structures are very unlikely capable of producing practical terahertz lasers, but their simplicity is an advantage in understanding the important mechanisms that determine the scattering rates between levels. This knowledge can now be transferred to more promising four subband structures.[4]

The results also showed that the 2111 Auger process dominated the electron-electron contribution to the w_{21} scattering rate, despite it transferring only a single electron compared to the two transferred by the 2211 rate. However, in the calculations relating to the prototype terahertz devices this electron-electron contribution was significantly smaller than the electron-phonon scattering rates.

The Pauli exclusion effect was shown to cause marked scattering rate suppression in the prototype terahertz devices between both laser subbands $|3\rangle$ and $|2\rangle$, as well as the laser ground level $|2\rangle$ and the lowest level $|1\rangle$. This was about an order of magnitude for the important 3121 electron-electron scattering rate, and up to a third for other rates in the $\Sigma n_i = 100\times10^{10}$ cm^{-2} case. Pauli exclusion has a minimal effect on the possibility of population inversion in our three level prototypes in the low electron density (10^{10} cm^{-2}) limit. However, for a four subband structure operating at the more practical higher densities,[4] these results demonstrate that Pauli exclusion will be important.

Finally, these conclusions led to an evaluation of the potential of optically pumped terahertz emitters based on the prototype devices that used a three-level asymmetric quantum-well structure. We calculated that it is still possible to achieve population inversion in these three-level systems at 50 K, but that the achievable inversion is strongly dependent on having a low electron density to reduce the $|3\rangle \rightarrow |2\rangle$ electron-electron scattering rates. Also, the results showed that there is an optimum combination of temperature and subband separation required to give the largest population ratio and hence best device performance.

*Electronic address: p.kinsler@elec-eng.leeds.ac.uk

[1] C. Sirtori, J. Faist, F. Capasso, D. L. Sivco, A. L. Hutchinson, and A. Y. Cho, Appl. Phys. Lett. **69**, 2810 (1996).
[2] *New Directions in Terahertz Technology*, edited by J. M. Chamberlain and R. E. Miles (Kluwer, Dordrecht, 1997).
[3] S. C. Lee, I. Galbraith, and C. R. Pidgeon, Phys. Rev. B **52**, 1874 (1995).
[4] P. Harrison and R. W. Kelsall, J. Appl. Phys. **81**, 7135 (1997).
[5] S. M. Goodnick and P. Lugli, Phys. Rev. B **37**, 2578 (1988).
[6] J. H. Smet, C. G. Fonstad, and Q. Hu, J. Appl. Phys. **79**, 9305 (1996).
[7] V. Berger, Semicond. Sci. Technol. **9**, 1493 (1994).
[8] A. Moskova and M. Mosko, Phys. Rev. B **49**, 7443 (1994); K. Kalna and M. Mosko, *ibid.* **54**, 17 730 (1996).
[9] B. K. Ridley, *Quantum Processes in Semiconductors* (Clarendon Press, Oxford, 1993).
[10] F. H. Julien, A. Sa'ar, J. Wang, and J. P. Leburton, Electron. Lett. **31**, 838 (1995).
[11] F. H. Julien, Z. Moussa, P. Boucaud, Y. Lavon, A. Sa'ar, J. Wang, J-P. Leburton, V. Berger, J. Nagle, and R. Planel, Superlattices Microstruct. **19**, 69 (1996).
[12] P. Harrison, W. E. Hagstron, and T. Stirner, Phys. Rev. B **47**, 16 404 (1993).
[13] M. Lundstrom, *Fundamentals of Carrier Transport* (Addison-Wesley, Redwood City, 1990).
[14] T. Piorek, Ph.D. thesis, University of Hull, U.K., 1996.
[15] B. K. Ridley, Phys. Rev. B **47**, 4592 (1993).
[16] B. K. Ridley, O. Al-Dossary, N. C. Constantinou, and M. Babiker, Phys. Rev. B **50**, 11 701 (1994).
[17] T. Ando, A. B. Fowler, and F. Stern, Rev. Mod. Phys. **54**, 437 (1982).
[18] P. F. Maldague, Surf. Sci. **73**, 296 (1978).
[19] S. C. Lee and I. Galbraith, Phys. Rev. B **55**, R16 025 (1997).
[20] S. Adachi, *Gallium Arsenide and Related Materials* (World Scientific, Singapore, 1994).